



CHORUS

This is the accepted manuscript made available via CHORUS. The article has been published as:

Enhanced antiferromagnetic resonance linewidth in NiO/Pt and NiO/Pd

Takahiro Moriyama, Kensuke Hayashi, Keisuke Yamada, Mitsuhiro Shima, Yutaka Ohya, Yaroslav Tserkovnyak, and Teruo Ono

Phys. Rev. B **101**, 060402 — Published 4 February 2020

DOI: [10.1103/PhysRevB.101.060402](https://doi.org/10.1103/PhysRevB.101.060402)

1 **Enhanced antiferromagnetic resonance linewidth in NiO/Pt and**
2 **NiO/Pd**

3
4 Takahiro Moriyama¹, Kensuke Hayashi², Keisuke Yamada², Mitsuhiro Shima²,
5 Yutaka Ohya², Yaroslav Tserkovnyak³ and Teruo Ono¹

6 ¹ *Institute for Chemical Research, Kyoto University, Gokasho, Uji, Kyoto, 611-0011, Japan.*

7 ² *Department of Materials Science and Processing, Graduate School of Natural Science and*
8 *Technology, Gifu University, Yanagido, Gifu City, Gifu 501-1193, Japan*

9 ³ *Department of Physics and Astronomy, University of California, Los Angeles, CA 90095, USA*

10
11 **Abstract**

12 In this letter, we investigate the enhancement of the antiferromagnetic damping in the
13 sintered NiO-HM granular systems having NiO/HM interfaces, where HM = Pt or Pd.

14 Under the assumption of the spin pumping model, we derive the effective interfacial
15 damping conductance g_{eff} , the parameter which characterizes the upper-bound
16 estimate of the spin pumping effect, to be $12 \pm 1 \text{ nm}^{-2}$ and $5 \pm 1 \text{ nm}^{-2}$ for the NiO/Pt and
17 the NiO/Pd interfaces, respectively, at room temperature. g_{eff} experimentally derived
18 in this study are an important milestone in antiferromagnetic spintronics, giving a
19 guideline for various spin current transfer and spin interaction phenomena with
20 antiferromagnets where the spin mixing conductance is involved.

1 A flow of electron spins, or spin current, exerts a torque on the local magnetization as
2 an important consequence of the interplay between the local magnetizations and the
3 itinerant electron spins [1]. By this so-called spin torque effect, one can manipulate the
4 magnetization directions [2] and even excite a persistent magnetization dynamics [3].
5 Most recently, it has been demonstrated that the same operation principle can be applied
6 to antiferromagnets which have no net magnetization but rather staggered microscopic
7 spins [4,5,6,7]. The spin torque effect is much appreciated in modern spintronic
8 applications [8], such as memory, logic, and high frequency devices, as it requires much
9 less energy to control the magnetization comparing to the traditional Ampere field.

10 On the other hand, the magnetization dynamics can create a flow of spin
11 current as a reciprocal process of the spin torque effect [9]. This so-called spin pumping
12 effect ejects the spin current (without any net charge current) into an adjacent material
13 in contact with the magnetic material under the magnetization dynamics. A consequence
14 of the spin pumping effect becomes noticeable when a non-magnetic heavy metal (HM)
15 with strong spin-orbit interaction is in contact, such as Pt or Pd. One of the significant
16 consequences is a broadening of the magnetic resonant linewidth [10]. When the
17 pumped spin current is dissipated by the adjacent material, the loss of the spin current,
18 or the loss of the spin angular momentum, results in an enhancement of damping of the
19 magnetic system and therefore the increase of the resonant linewidth. Alternatively, the
20 pumped spin current can be electrically detected via the inverse spin Hall effect (ISHE)
21 [11], which adds a great potential to the spin pumping effect not only toward application
22 [12] but also for a sensitive probe of various spin-orbit related phenomena [13,14].

23 Since it is generally convenient to excite steady magnetization dynamics in
24 order to observe the spin pumping effect, almost all the spin pumping experiments have

1 so far been investigated with ferromagnetic materials at the ferromagnetic resonant
2 frequency in a GHz range by using well established microwave electronics. However, in
3 conjunction with the recently emerging antiferromagnetic spintronics [15,16], there is a
4 growing interest in the spin pumping effect in antiferromagnetic materials with the Néel
5 order dynamics in a THz frequency range [17,18,19,20] , which can open up a new
6 realm of *THz spintronics* leading to novel THz spin devices [21,22] and leading to
7 improved understanding of the ultra-high speed spin phenomena in magnetism. While
8 the spin pumping effect in ferromagnets is well understood from both experimental and
9 theoretical points of views, lack of experimental demonstrations of the
10 antiferromagnetic spin pumping effect, in spite of recent intensive theoretical efforts
11 [17,18,19,20], impedes further advancement of antiferromagnetic spintronics toward
12 THz spintronics.

13 In this report, we investigate the enhanced damping in antiferromagnets at the
14 THz resonant frequency. The continuous wave (CW)-THz spectroscopy revealed that
15 the magnetic damping of the sintered NiO-HM granular systems, where HM = Pt or Pd,
16 is enhanced due to the NiO/HM interface, which suggests the spin pumping effect. The
17 effective interfacial damping conductance g_{eff} , derived under assumption that the
18 whole damping enhancement would be due to the spin pumping effect, is found to be
19 $g_{eff} = 12 \pm 1 \text{ nm}^{-2}$ and $5 \pm 1 \text{ nm}^{-2}$ for the NiO/Pt and the NiO/Pd interfaces, respectively,
20 at room temperature. The trend of g_{eff} is consistent with the ferromagnetic/HM case
21 where the Pd interface generally exhibits smaller g_{eff} than the Pt interface [9,23,24].

22 First, we try to formulate the damping variation, under the assumption of the
23 spin pumping model, with antiferromagnetic NiO and the HM as depicted in Fig. 1 (a).
24 NiO is antiferromagnetic below the Néel temperature $T_N = 523 \text{ K}$ and is a rock-salt

1 structure with a slight rhombohedral distortion [25]. In the ground state, the Ni^{2+} spins
 2 align ferromagnetically in a $\{111\}$ plane and are antiferromagnetically coupled between
 3 adjacent $\{111\}$ planes, resulting in a strong *easy-plane* anisotropy in a $\{111\}$ plane and
 4 a weak three-fold *in-plane* anisotropy in the $\langle 11\bar{2} \rangle$ directions in the $\{111\}$ plane.

5 Magnetization dynamics of the antiferromagnetic NiO can be described by the
 6 following Lagrangian density based on the conventional sigma model [26,27],

$$\mathcal{L}[\mathbf{n}] = \frac{\chi_{\perp}}{2} (\partial_t \mathbf{n} + \mathbf{n} \times \gamma \mathbf{B})^2 - \frac{A}{2} (\partial_t \mathbf{n})^2 - \frac{K_1 n_x^2 + K_2 n_y^2}{2}, \quad (1)$$

7 where $|\mathbf{n}| \equiv 1$ is the directional Néel order and K_1 and K_2 are the out-of-easy-plane
 8 and in-plane anisotropy energy, respectively, with $K_1 \gg K_2$. Note that in the cartesian
 9 coordinate we set the y - z plane as the easy plane within which the Néel order prefers to
 10 orient along the z axis. $\gamma = 1.76 \times 10^{11} \text{ T}^{-1}\text{s}^{-1}$ is the gyromagnetic ratio and χ_{\perp} is the
 11 perpendicular spin susceptibility. \mathbf{B} is the applied magnetic field. Below, we discuss the
 12 natural modes of magnetic dynamics in the absence of a static magnetic field and we
 13 ignore K_2 in line with our experiments described below. The dissipation is described by
 14 the following Rayleigh function [28],

$$\mathcal{R}[\partial_t \mathbf{n}] = \frac{\alpha s}{2} (\partial_t \mathbf{n})^2, \quad (2)$$

15 where,

$$\alpha = \alpha_0 + \frac{\hbar g_{eff}^{\uparrow\downarrow}}{4\pi s} \frac{S}{V_{NiO}}. \quad (3)$$

16 α_0 is the intrinsic damping. The second term representing the spin pumping enhanced
 17 damping is derived from the total spin current dissipation \mathbf{I}_s which is the sum of the
 18 pumped spin current $\mathbf{I}_s^{\text{pump}}$ and the back flow spin current \mathbf{I}_s^0 as $\mathbf{I}_s = \mathbf{I}_s^{\text{pump}} + \mathbf{I}_s^0$
 19 (see Fig. 1 (a)). $g_{eff}^{\uparrow\downarrow}$ is the effective spin mixing conductance at the NiO/HM interface
 20 solely characterizing the spin pumping effect, s is the full saturated spin density of

1 magnetic sublattices, S is the interface area, and V_{NiO} is the volume of the NiO. By
 2 solving the Euler-Lagrange equation with the Lagrangian density in Eq. 1 and the
 3 dissipation term in Eq. 2, the (linearly-polarized) small-angle Néel vector dynamics can
 4 eventually be written as the damped oscillator equation as [29],

$$\ddot{n} + \Delta\omega\dot{n} + \omega^2n = 0 \quad (4)$$

5 where the resonant frequency ω and the resonant linewidth (full width at half
 6 maximum) $\Delta\omega$ are respectively,

$$\omega = \sqrt{K_1/\chi_\perp}, \quad (5)$$

7 and,

$$\Delta\omega = \alpha S/\chi_\perp. \quad (6)$$

8 With Eqs. 3 and 6, we can therefore characterize the spin pumping effect from the
 9 resonant linewidth of the antiferromagnetic resonance.

10 The samples used in this experiment are sintered pellets of NiO with the
 11 inclusion of HM granules, referred to as the NiO-HM granular pellets, synthesized from
 12 a mixture of NiO and Pt or Pd powder (See Supplementary Information (SI) for a
 13 detailed sample preparation procedure [29]). We vary the S/V_{NiO} ratio by varying the
 14 composition of the pellets to be $(NiO)_{1-x}HM_x$ ($x = 0, 0.02, 0.05, 0.08, \text{ and } 0.10$). We
 15 hereafter refer to Pt and Pd composition as x_{Pt} and x_{Pd} , respectively. Table 1 shows the
 16 packing ratio for each pellet which is the ratio of the measured pellet density to the
 17 nominal density calculated for the given composition of NiO (6.67 g/cm^3), Pt (21.5
 18 g/cm^3), and Pd (12.0 g/cm^3). The packing ratio less than unity indicates that the pellets
 19 contain air pores. We also prepared some control samples, in which the air pore
 20 composition x_p of NiO pellet is deliberately varied [29], in order to elucidate the effect
 21 of the HM granules by comparing with the *air granules*, *i.e.* air pores. THz wave

1 transmission through the granular pellets was measured by using a frequency domain
 2 CW-THz spectroscopy system [30,31] capable of scanning up to 2 THz as the schematic
 3 illustration is shown in Fig. 1(b). The absorption peak due to the antiferromagnetic
 4 resonance is expected in the transmission spectra. The temperature of the sample can be
 5 controlled between 300K and 440K. We apply no magnetic field in the measurements.

6 Figure 2 shows the optical microscope images of the polished surface of the
 7 NiO-HM granular pellets. Randomly dispersed HM granules are seen in the brightest
 8 color in the NiO matrix (the second brightest regions). The darkest regions are due to
 9 the surface roughness developed by surface abrasions during the polishing process (The
 10 raw images are found in SI [29]). The HM granule regions are filled with red in Figs. 2
 11 (b-e) and (j-m) to make them more visible. Figs. 2 (f-i) and (n-q) show the
 12 corresponding histograms of the nominal diameter d_n of the granule (see SI for the
 13 analysis of d_n). The average diameter of the HM granules d_{ave} were estimated and are
 14 summarized in Table. 1.

15

16 Table 1 Packing ratio and average diameter of the Pt and Pd granules for various
 17 composition x_{Pt} and x_{Pd} .

x_{Pt}	0.00	0.02	0.05	0.08	0.10
Packing ratio	0.96 ± 0.01	0.97 ± 0.01	0.95 ± 0.01	0.95 ± 0.01	0.98 ± 0.01
d_{ave} (μm)	0	0.65	0.75	0.97	1.12
x_{Pd}		0.02	0.05	0.08	0.10
Packing ratio		0.95 ± 0.01	0.95 ± 0.01	0.94 ± 0.01	0.95 ± 0.01
d_{ave} (μm)		0.90	1.15	1.21	1.32

18

19

20 Figure 3 shows the X-ray diffraction (XRD) of the NiO-Pt and the NiO-Pd

1 granular pellets with different compositions. We find two separate phases of pure NiO
 2 and pure Pt or pure Pd without any other impurity phases (see SI for more extensive
 3 investigations on the intermixing [29]). The diffraction linewidths for the NiO, the Pt,
 4 and the Pd are too narrow to be analyzed by the Scherrer equation, giving only a rough
 5 estimation for the crystal grain size being >100 nm with which the finite-size effect is
 6 negligible [32]. There are no appreciable differences in the peak position (see the insets
 7 of Fig. 3) as well as the linewidths in all the samples, suggesting the inclusion of the
 8 HM granules does not influence the crystalline structures of the NiO.

9 The antiferromagnetic resonant mode at ~ 1 THz, corresponding to the
 10 out-of-the-easy-plane mode [27], was seen in the transmission spectra for all the
 11 samples at room temperature and no other modes are apparent in the range of $0.1 \sim 2$
 12 THz. The temperature dependence of the resonant frequency shown in Fig. 4 is nearly
 13 same for all the samples, indicating that the HM granules in the NiO matrix do not
 14 influence the magnetic susceptibility, or the exchange constant [33], and the
 15 out-of-the-easy-plane anisotropy both of which are relevant to the resonant frequency
 16 [31]. The Néel temperature and the resonant frequency at 0 K are estimated to be $T_N =$
 17 521 ± 2 K and $\omega_0/(2\pi) = 1.095 \pm 0.002$ THz, respectively, by the equation $\omega =$
 18 $\omega_0(M_0'(T))^n$ where $M_0'(T)$ is the normalized sublattice magnetization computed by
 19 the Brillouin function $B_{S=1}(T)$ and $n = 0.72$ is the exponent for NiO [30,33]. These
 20 results prove that the quality of the NiO matrix is the same regardless of the HM
 21 granule inclusions. The resonant linewidth $\Delta\omega$ is obtained by fitting the absorption
 22 peak at 300K with the Lorentzian function as shown in Fig. 5. By using the measured
 23 susceptibility $\chi = (1.49 \pm 0.01)\hbar \times 10^{-13}$ s/nm³ which translates to $\chi_{\perp} =$
 24 $(3/2)\chi = (2.24 \pm 0.01)\hbar \times 10^{-13}$ s/nm³ [29] and $s = 27\hbar$ nm⁻³ [25] for the NiO, the

1 damping constant α is estimated by Eq. 6 and is shown in Fig. 6 (a). It is evident that
2 the $\Delta\omega$ and α increases with increasing both x_{Pt} and x_{Pd} . α increases much more
3 rapidly with the Pt granular than the Pd granular.

4 We now address some caveats concerning the antiferromagnetic spin pumping
5 model. We first need to assure that the increase of the $\Delta\omega$ and α are solely due to the
6 effect of the HM granules. The major concern is extrinsic contributions to the damping,
7 such as the inhomogeneous broadening [31], due to the inclusion of the HM granules. It
8 is known that this extrinsic contribution can vary depending on the quality of the sample,
9 such as defects, inhomogeneities, and crystallinity. The effect of crystallinity can be
10 insignificant since the XRD indicates that the NiO maintains its inherent crystal
11 structure regardless of the HM granular inclusions (see Fig. 3). On the other hand, a
12 control experiment is necessary to address the effect of HM granules viewed as defects
13 and inhomogeneities in the NiO pellet. In order to create control samples with the same
14 defects and inhomogeneities but without the HM granules, we prepared the NiO pellets
15 with air pores, or *air granules*, the density x_p of which is in the same range as the HM
16 granules (See SI for the exact definition of x_p [29]). As the obtained $\Delta\omega$ and α almost
17 stay constant with respect to x_p (see Fig. 6(a)), the defects and inhomogeneities by the
18 air granules do not significantly contribute to the damping, which therefore ensures that
19 the damping enhancement is predominantly due to the HM. **We should note that our
20 experimental setup does not have a mechanism to clearly distinguish the non-local
21 effect, i.e. the spin pumping effect, from other “local” effects, such as magnetic
22 proximity effect, the spin memory loss [23,24], and the interfacial incoherent magnons
23 [34,35], which could contribute to the damping enhancement. All these parasitic effects
24 are inherently absorbed into the enhancement of our effective interfacial damping**

1 conductance g_{eff} ($\geq g_{eff}^{\uparrow\downarrow}$).

2 For convenience in analyzing the experimental data, we can rewrite Eq. 3 by
3 taking into account the distribution of the nominal granular diameter d_n and the
4 enhanced damping $\Delta\alpha = \alpha - \alpha_0 - \alpha_p(x)$ with $\alpha_0 = 7.4 \times 10^{-4}$ of $x = 0$ and the
5 damping increase in air granular sample $\alpha_p(x)$ as,

$$\Delta\alpha = \frac{3\hbar g_{eff}}{2\pi s} (x + x^2) \frac{\sum_n d_n^2 f_n}{\sum_n d_n^3} \quad (7)$$

6 where f_n is a factor relating the surface area of the ideal spherical granule with the
7 diameter d to that of the actual irregular granule, which can be experimentally obtained
8 from the image analysis of Fig. 2 (see SI for more detailed derivation of Eq. 7 [29]).

9 Note that, from now on, we use $g_{eff}^{\uparrow\downarrow}$ to absorb the parasitic effects.

10 Figure 6 (b) shows $\Delta\alpha$ as a function of $(x + x^2)\Gamma$, where
11 $\Gamma = \sum_n d_n^2 f_n / \sum_n d_n^3$. The fitting with Eq. 7 yields the effective interfacial damping
12 conductance to be $g_{eff} = 12 \pm 1 \text{ nm}^{-2}$ and $5 \pm 1 \text{ nm}^{-2}$ for the NiO/Pt and the NiO/Pd
13 interfaces, respectively. The effective spin mixing conductance $g_{eff}^{\uparrow\downarrow}$ for
14 antiferromagnets is generally expected to be of the same order of magnitude as the
15 ferromagnetic counterpart [17], *i.e.* $\sim 10 \text{ nm}^{-2}$, and similarly to the ferromagnetic case it
16 is sensitive to interface quality. Most importantly, the Pd interface exhibits smaller g_{eff}
17 than the Pt interface, which is in line with the $g_{eff}^{\uparrow\downarrow}$ behavior in the ferromagnetic/HM
18 case. The latter is conventionally related to the spin-sink properties of the normal metal,
19 as well as the magnetic proximity effect and spin relaxation at the interface [9,23,24].
20 Therefore, the trend of g_{eff} in the NiO/Pt and the NiO/Pd cases suggests that the spin
21 pumping effect is present at the NiO/HM interface.

22 The g_{eff} found in this study, in a good agreement with a general rough
23 theoretical estimate of the effective spin mixing conductance $g_{eff}^{\uparrow\downarrow} \sim 10 \text{ nm}^{-2}$ for

1 antiferromagnets [5,17,18,19,36], is an important milestone in antiferromagnetic
2 spintronics and particularly gives guidelines for various spin current transfer and spin
3 interaction phenomena with antiferromagnets which has recently been studied
4 vigorously [4,5,36,37,38]. The most fascinating aspect of the antiferromagnetic spin
5 pumping effect is the electrical detection of the antiferromagnetic spin dynamics in
6 combination with ISHE, which leads to antiferromagnetic THz spin devices
7 [17,18,19,20]. It, however, remains more challenging to realize an appreciable spin
8 pumping voltage signal than to detect the damping enhancement in the present work
9 since the former is proportional to θ^2 , where θ is the cone angle of the precessing Néel
10 order which is generally expected to be much smaller than the ferromagnetic case [18].
11 We also note that, while the present experiments rely on the bulk THz absorption, it
12 should be important in the interest of THz spintronics to develop those mechanisms
13 suitable for thin film antiferromagnet systems.

14 In summary, we investigated the enhancement of antiferromagnetic damping in
15 the NiO/HM system. Under the assumption of the spin pumping model, we estimate the
16 effective interfacial damping conductance of the NiO/Pt and NiO/Pd interface to be
17 $g_{eff} = 12 \pm 1 \text{ nm}^{-2}$ and $5 \pm 1 \text{ nm}^{-2}$, respectively. Our experimental results suggest the
18 missing part of the spin interaction physics in antiferromagnets at THz, *i.e.* the spin
19 pumping effect, among other possible parasitic effects such as the proximity effect and
20 the spin memory loss. Although more intensive development should be necessary to
21 demonstrate the electrical detection of the spin pumping effect with ISHE, which is
22 challenging yet the most fascinating aspect of the antiferromagnetic spin pumping effect
23 leading to THz spin devices [17,18,19,20], the present work which experimentally
24 estimates g_{eff} encourages such research direction. Furthermore, the experimental

1 manifestation of the value of g_{eff} helps understanding various spin current transfer
2 and spin interaction phenomena with antiferromagnets, and would further motivate and
3 promote the antiferromagnetic spintronics.
4
5
6
7

8 **Acknowledgements**

9 This work was supported in part by JSPS KAKENHI Grant Numbers 17H04924,
10 15H05702, 17H04795, 17H05181 (“Nano Spin Conversion Science”), by the
11 Collaborative Research Program of Institute for Chemical Research, Kyoto University
12 (grant # 2018-61 and 2019-87), and by the U.S. Department of Energy, Office of Basic
13 Energy Sciences, Division of Materials Science and Engineering under Award No.
14 DE-SC0012190 (Y.T.).
15
16

1 **Figure captions:**

2 **Fig. 1** THz spectroscopy measurements and spin pumping in the NiO/HM system. (a)
3 The precessing Néel order $\mathbf{n}(t)$ in the NiO with the volume V_{NiO} pumps the spin current
4 \mathbf{I}_s^{Pump} into the HM with the contact area S and the effective spin mixing
5 conductance $g_{eff}^{\uparrow\downarrow}$. The resulting backflow spin current \mathbf{I}_s^0 in turn flows back into the
6 NiO. (b) Schematic illustration of the CW-THz spectroscopy setup measuring the THz
7 wave transmission through the $(NiO)_{1-x}HM_x$ samples.

8
9 **Fig. 2** Optical microscope images of the surface of the $(NiO)_{1-x}HM_x$ samples. The
10 polished surfaces of the $(NiO)_{1-x}Pt_x$ and $(NiO)_{1-x}Pd_x$ samples are shown in (a-e) and
11 (j-m), respectively. Size of the scale bars is 25 μm . The HM granular areas are spotted
12 by red by the image analysis described in SI. The corresponding histograms of the
13 nominal granular diameter d_n are shown in (f-i) and (n-q).

14
15 **Fig. 3** X-ray diffraction (XRD) and antiferromagnetic resonance. (a) XRD of the
16 $(NiO)_{1-x}Pt_x$ samples. (b) XRD of the $(NiO)_{1-x}Pd_x$ samples. The insets magnify and
17 superpose the NiO (200) peaks of all the compositions.

18
19 **Fig. 4** Transmission spectra of (a) the $(NiO)_{1-x}Pt_x$ and (c) $(NiO)_{1-x}Pd_x$ the samples as
20 functions of frequency and temperature. The resonant frequency as a function of
21 temperature for (b) the $(NiO)_{1-x}Pt_x$ and (d) the $(NiO)_{1-x}Pd_x$ samples. The inset in (b) and
22 (d) superposes the resonant frequency of all the $(NiO)_{1-x}HM_x$ samples and the fitting
23 curve to obtain T_N and ω_0 .

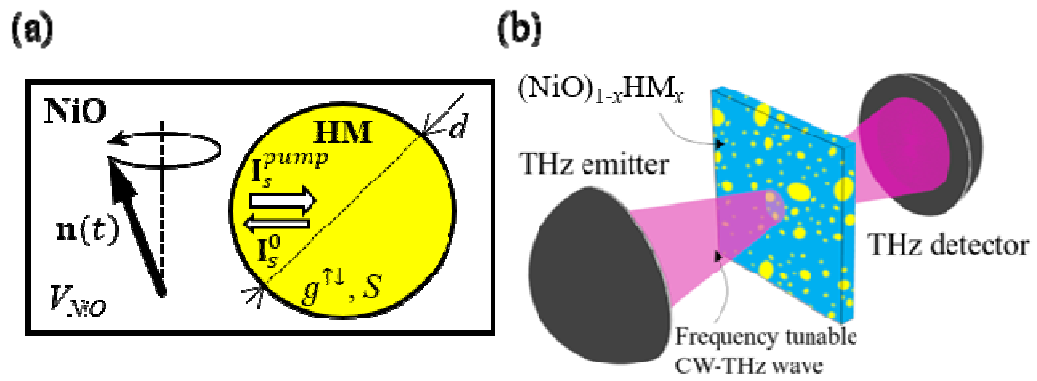
24 **Fig. 5** x dependence of the transmittance spectra for (a) the $(NiO)_{1-x}Pt_x$ and (b)

1 (NiO)_{1-x}Pd_x. The dotted curve is the Lorentzian fitting from which the linewidth $\Delta\omega$ is
2 obtained.

3

4 **Fig. 6** (a) Linewidth $\Delta\omega$ and damping α as a function of x with the Pt, Pd, and air
5 granules. The dotted curve is an eye guide. (b) $\Delta\alpha$ as a function of $(x + x^2)\Gamma$ fitted
6 with Eq. 7 to obtain g_{eff} .

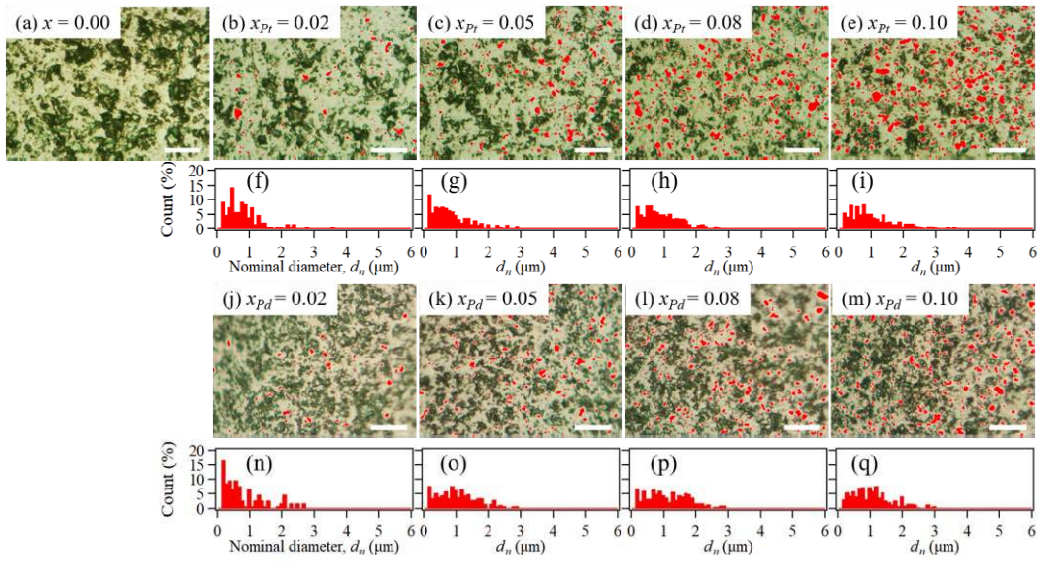
7



1

2 Figure 1 Moriyama et al.

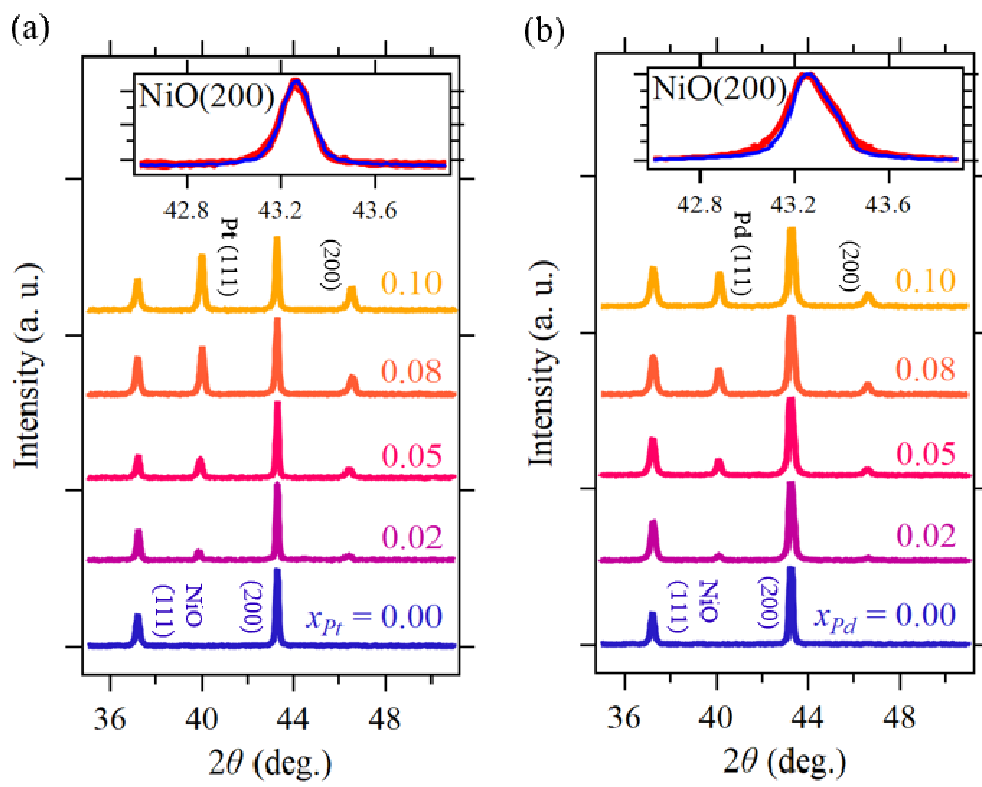
3



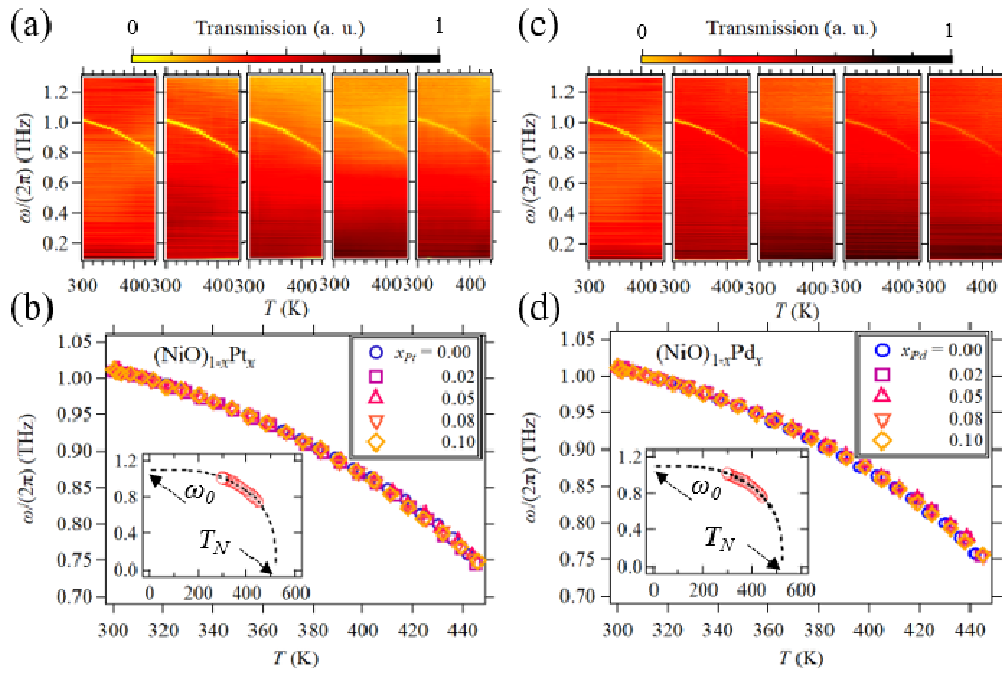
1

2 Figure 2 Moriyama et al.

3

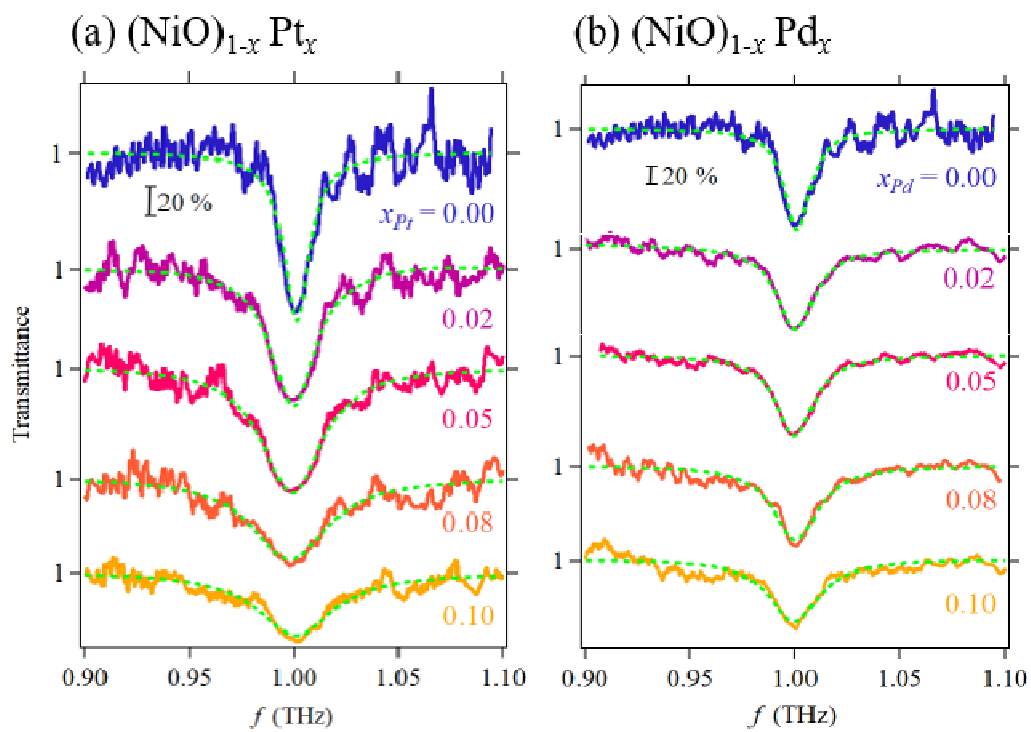


1
 2 Figure 3 Moriyama et al.
 3



1
2
3

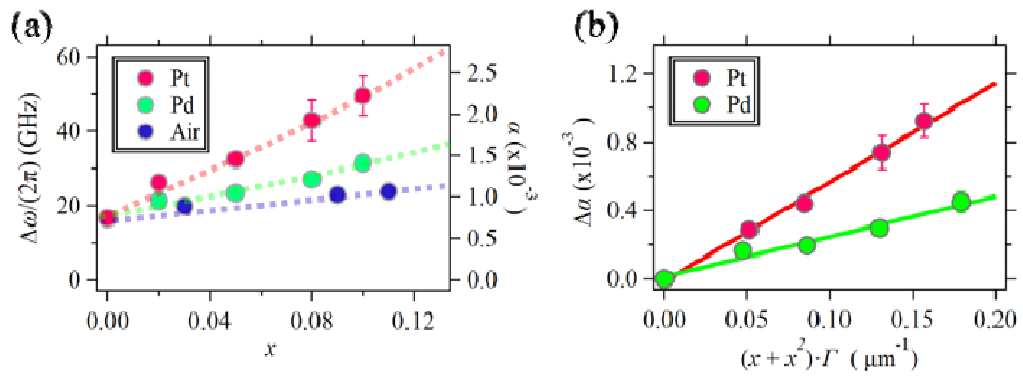
Figure 4 Moriyama et al.



1

2 Figure 5 Moriyama et al.

3



1
2
3
4

Figure 6 Moriyama et al.

1 References:

-
- [1] D. C. Ralph and M. D. Stiles, *J. Magn. Magn. Mater.* **320**, 1190 (2008).
- [2] E. B. Myers, D. C. Ralph, J. A. Katine, R. N. Louie, and R. A. Buhrman, *Science* **285**, 867 (1999).
- [3] S. I. Kiselev, J. C. Sankey, I. N. Krivorotov, N. C. Emley, R. J. Schoelkopf, R. A. Buhrman, and D. C. Ralph, *Nature* **425**, 380 (2003).
- [4] X. Z. Chen, R. Zarzuela, J. Zhang, C. Song, X. F. Zhou, G. Y. Shi, F. Li, H. A. Zhou, W. J. Jiang, F. Pan, and Y. Tserkovnyak, *Phys. Rev. Lett.* **120**, 207204 (2018).
- [5] T. Moriyama, K. Oda, T. Ohkochi, M. Kimata, and T. Ono, *Sci. Rep.* **8**, 14167 (2018).
- [6] P. Wadley, B. Howells, J. Elezny, C. Andrews, V. Hills, R. P. Campion, V. Novak, K. Olejnik, F. Maccherozzi, S. S. Dhesi, S. Y. Martin, T. Wagner, J. Wunderlich, F. Freimuth, Y. Mokrousov, J. Kune, J. S. Chauhan, M. J. Grzybowski, A. W. Rushforth, K. W. Edmonds, B. L. Gallagher, and T. Jungwirth, *Science* **351**, 587 (2016).
- [7] T. Moriyama, W. Zhou, T. Seki, K. Takanashi, and T. Ono, *Phys. Rev. Lett.* **121**, 167202 (2018).
- [8] N. Locatelli, V. Cros, and J. Grollier, *Nat. Mater.* **13**, 11 (2013).
- [9] Y. Tserkovnyak, A. Brataas, G. E. W. Bauer, and B. I. Halperin, *Rev. Mod. Phys.* **77**, 1375 (2005).
- [10] S. Mizukami, Y. Ando and T. Miyazaki, *Jpn. J. Appl. Phys.* **40**, 580 (2001).
- [11] E. Saitoh, M. Ueda, H. Miyajima, and G. Tatara, *Appl. Phys. Lett.* **88**, 15 (2006).
- [12] A. Brataas, Y. Tserkovnyak, G. E. W. Bauer, and B. I. Halperin, *Phys. Rev. B* **66**, 604041 (2002).
- [13] K. Ando, S. Takahashi, J. Ieda, Y. Kajiwara, H. Nakayama, T. Yoshino, K. Harii, Y. Fujikawa, M. Matsuo, S. Maekawa, and E. Saitoh, *J. Appl. Phys.* **109**, 103913 (2011).
- [14] J. C. Rojas Sánchez, L. Vila, G. Desfonds, S. Gambarelli, J. P. Attané, J. M. De Teresa, C. Magén, and A. Fert, *Nat. Commun.* **4**, 1 (2013).
- [15] T. Jungwirth, X. Marti, P. Wadley, and J. Wunderlich, *Nat. Nanotechnol.* **11**, 231 (2016).
- [16] V. Baltz, A. Manchon, M. Tsoi, T. Moriyama, T. Ono, and Y. Tserkovnyak, *Rev. Mod. Phys.* **90**, 015005 (2018).
- [17] S. Takei, B. I. Halperin, A. Yacoby, and Y. Tserkovnyak, *Phys. Rev. B* **90**, 094408 (2014).
- [18] R. Cheng, J. Xiao, Q. Niu, and A. Brataas, *Phys. Rev. Lett.* **113**, 1 (2014).
- [19] Ø. Johansen and A. Brataas, *Phys. Rev. B* **95**, 1 (2017).
- [20] S. A. Gulbrandsen and A. Brataas, *Phys. Rev. B* **97**, (2018).
- [21] J. Walowski and M. Münzenberg, *J. of Appl. Phys.* **120**, 140901 (2016).
- [22] D. M. Mittleman, *J. of Appl. Phys.* **122**, 230901 (2017).
- [23] Y. Liu, Z. Yuan, R. J. H. Wesselink, A. A. Starikov, and P. J. Kelly, *Phys. Rev. Lett.* **113**, 207202 (2014).
- [24] M. Caminale, A. Ghosh, S. Auffret, U. Ebels, K. Ollefs, F. Wilhelm, A. Rogalev, and W. E. Bailey, *Phys. Rev. B* **94**, 014414 (2016).
- [25] M. T. Hutchings and E. J. Samuelsen, *Phys. Rev. B* **6**, 3447 (1972).
- [26] A. F. Andreev and V. I. Marchenko, *Sov. Phys. Uspekhi* **23**, 21 (1980).
- [27] T. Satoh, S.-J. Cho, R. Iida, T. Shimura, K. Kuroda, H. Ueda, Y. Ueda, B. A. Ivanov, F. Nori, and M. Fiebig, *Phys. Rev. Lett.* **105**, 077402 (2010).
- [28] Y. Tserkovnyak and H. Ochoa, *Phys. Rev. B* **96**, 100402 (2017).
- [29] See Supplementary Information at [URL] for extended description and data.
- [30] A. Roggenbuck, H. Schmitz, A. Deninger, I. C. Cámara Mayorga, J. Hemberger, R. Güsten, and M. Grüninger, *New J. Phys.* **12**, 043017 (2010).
- [31] T. Moriyama, K. Hayashi, K. Yamada, M. Shima, Y. Ohya, and T. Ono, *Phys. Rev. Mater.* **3**,

051402 (2019).

[32] R. H. Kodama, Salah A. Makhoul, and A. E. Berkowitz, Phys. Rev. Lett. **79**, 1393 (1997).

[33] A. Sievers and M. Tinkham, Phys. Rev. **129**, 1566 (1963).

[34] B. Flebus, P. Upadhyaya, R. A. Duine, and Y. Tserkovnyak, Phys. Rev. B **94**, 214428 (2016).

[35] C. Du, T. van der Sar, T. X. Zhou, P. Upadhyaya, F. Casola, H. Zhang, M. C. Onbasli, C. A. Ross, R. L. Walsworth, Y. Tserkovnyak, A. Yacoby, Science **357**, 195 (2017).

[36] H. Wang, C. Du, P. C. Hammel, and F. Yang, Phys. Rev. Lett. **113**, 097202 (2014).

[37] C. Hahn, G. Loubens, V. V. Naletov, J. B. Youssef, O. Klein, and M. Viret, Europhys. Lett. **108**, 57005 (2014).

[38] T. Moriyama, S. Takei, M. Nagata, Y. Yoshimura, N. Matsuzaki, T. Terashima, Y. Tserkovnyak, and T. Ono, Appl. Phys. Lett. **106**, 162406 (2015).